arXiv:2506.11688v2 [astro-ph.HE] 28 Oct 2025

The Energy Spectrum of Ultra-High Energy Cosmic Rays across Declinations −90° to +44.8° as measured at the Pierre Auger Observatory

A. Abdul Halim,[1] P. Abreu,[2] M. Aglietta,[3,4] I. Allekotte,[5] K. Almeida Cheminant,[6,7] A. Almela,[8,9] R. Aloisio,[10,11] J. Alvarez-Muñiz,[12] A. Ambrosone,[10] J. Ammerman Yebra,[12] G.A. Anastasi,[13,14] L. Anchordoqui,[15] B. Andrada,[8] L. Andrade Dourado,[10,11] S. Andringa,[2] L. Apollonio,[16,17] C. Aramo,[18] E. Arnone,[19,4] J.C. Arteaga Velázquez,[20] P. Assis,[2] G. Avila,[21] E. Avocone,[22,11] A. Bakalova,[23] F. Barbato,[10,11] A. Bartz Mocellin,[24] J.A. Bellido,[1] C. Berat,[25] M.E. Bertaina,[19,4] M. Bianciotto,[19,4] P.L. Biermann,[26] V. Binet,[27] K. Bismark,[28,8] T. Bister,[7,6] J. Biteau,[29,30] J. Blazek,[23] J. Blümer,[31] M. Boháčová,[23] D. Boncioli,[22,11] C. Bonifazi,[32] L. Bonneau Arbeletche,[33] N. Borodai,[34] J. Brack,[35] P.G. Brichetto Orchera,[8,31] F.L. Briechle,[36] A. Bueno,[37] S. Buitink,[38] M. Buscemi,[14,13] M. Büsken,[28,8] A. Bwembya,[7,6] K.S. Caballero-Mora,[39] S. Cabana-Freire,[12] L. Caccianiga,[16,17] F. Campuzano,[40] J. Caraça-Valente,[24] R. Caruso,[13,14] A. Castellina,[3,4] F. Catalani,[41] G. Cataldi,[42] L. Cazon,[12] M. Cerda,[43] B. Čermáková,[31] A. Cermenati,[10,11] J.A. Chinellato,[33] J. Chudoba,[23] L. Chytka,[44] R.W. Clay,[1] A.C. Cobos Cerutti,[40] R. Colalillo,[45,18] R. Conceição,[2] G. Consolati,[17,46] M. Conte,[47,42] F. Convenga,[22,11] D. Correia dos Santos,[48] P.J. Costa,[2] C.E. Covault,[49] M. Cristinziani,[50] C.S. Cruz Sanchez,[51] S. Dasso,[52,53] K. Daumiller,[31] B.R. Dawson,[1] R.M. de Almeida,[48] E.-T. de Boone,[50] B. de Errico,[48] J. de Jesús,[8,31] S.J. de Jong,[7,6] J.R.T. de Mello Neto,[48] I. De Mitri,[10,11] J. de Oliveira,[54] D. de Oliveira Franco,[55] F. de Palma,[47,42] V. de Souza,[56] E. De Vito,[47,42] A. Del Popolo,[13,14] O. Deligny,[57] N. Denner,[23] L. Deval,[3,4] A. di Matteo,[4] C. Dobrigkeit,[33] J.C. D'Olivo,[58] L.M. Domingues Mendes,[59,2] Q. Dorosti,[50] J.C. dos Anjos,[59] R.C. dos Anjos,[60] J. Ebr,[23] F. Ellwanger,[31] R. Engel,[28,31] I. Epicoco,[47,42] M. Erdmann,[36] A. Etchegoyen,[8,9] C. Evoli,[10,11] H. Falcke,[7,61,6] G. Farrar,[62] A.C. Fauth,[33] T. Fehler,[50] F. Feldbusch,[63] A. Fernandes,[2] M. Fernandez,[64] B. Fick,[65] J.M. Figueira,[8] P. Filip,[28,8] A. Filipčič,[66,67] T. Fitoussi,[31] B. Flaggs,[68] T. Fodran,[7] A. Franco,[42] M. Freitas,[2] T. Fujii,[69,70] A. Fuster,[8,9] C. Galea,[7] B. García,[40] C. Gaudu,[71] P.L. Ghia,[57] U. Giaccari,[42] F. Gobbi,[43] F. Gollan,[8] G. Golup,[5] M. Gómez Berisso,[5] P.F. Gómez Vitale,[21] J.P. Gongora,[21] J.M. González,[5] N. González,[8] D. Góra,[34] A. Gorgi,[3,4] M. Gottowik,[31] F. Guarino,[45,18] G.P. Guedes,[72] E. Guido,[50] L. Gülzow,[31] S. Hahn,[28] P. Hamal,[23] M.R. Hampel,[8] P. Hansen,[51] V.M. Harvey,[1] A. Haungs,[31] T. Hebbeker,[36] C. Hojvat,[73] J.R. Hörandel,[7,6] P. Horvath,[44] M. Hrabovský,[44] T. Huege,[31,38] A. Insolia,[13,14] P.G. Isar,[74] M. Ismaiel,[7,6] P. Janecek,[23] V. Jilek,[23] K.-H. Kampert,[71] B. Keilhauer,[31] A. Khakurdikar,[7] V.V. Kizakke Covilakam,[8,31] H.O. Klages,[31] M. Kleifges,[63] J. Köhler,[31] F. Krieger,[36] M. Kubatova,[23] N. Kunka,[63] B.L. Lago,[75] N. Langner,[36] N. Leal,[8] M.A. Leigui de Oliveira,[76] Y. Lema-Capeans,[12] A. Letessier-Selvon,[77] I. Lhenry-Yvon,[57] L. Lopes,[2] J.P. Lundquist,[67] M. Mallamaci,[78,14] D. Mandat,[23] P. Mantsch,[73] F.M. Mariani,[16,17] A.G. Mariazzi,[51] I.C. Mariş,[64] G. Marsella,[78,14] D. Martello,[47,42] S. Martinelli,[31,8] M.A. Martins,[12] H.-J. Mathes,[31] J. Matthews,[79] G. Matthiae,[80,81] E. Mayotte,[24] S. Mayotte,[24] P.O. Mazur,[73] G. Medina-Tanco,[58] J. Meinert,[71] D. Melo,[8] A. Menshikov,[63] C. Merx,[31] S. Michal,[23] M.I. Micheletti,[27] L. Miramonti,[16,17] M. Mogarkar,[34] S. Mollerach,[5] F. Montanet,[25] L. Morejon,[71] K. Mulrey,[7,6] R. Mussa,[4] W.M. Namasaka,[71] S. Negi,[23] L. Nellen,[58] K. Nguyen,[65] G. Nicora,[82] M. Niechciol,[50] D. Nitz,[65] D. Nosek,[83] A. Novikov,[68] V. Novotny,[83] L. Nožka,[44] A. Nucita,[47,42] L.A. Núñez,[84] J. Ochoa,[8,31] C. Oliveira,[56] L. Östman,[23] M. Palatka,[23] J. Pallotta,[82] S. Panja,[23] G. Parente,[12] T. Paulsen,[71] J. Pawlowsky,[71] M. Pech,[23] J. Pękala,[34] R. Pelayo,[85] V. Pelgrims,[64] L.A.S. Pereira,[86] E.E. Pereira Martins,[28,8] C. Pérez Bertolli,[8,31] L. Perrone,[47,42] S. Petrera,[10,11] C. Petrucci,[22] T. Pierog,[31] M. Pimenta,[2] M. Platino,[8] B. Pont,[7] M. Pourmohammad Shahvar,[78,14] P. Privitera,[69] C. Priyadarshi,[34] M. Prouza,[23] K. Pytel,[87] S. Querchfeld,[71] J. Rautenberg,[71] D. Ravignani,[8] J.V. Reginatto Akim,[33] A. Reuzki,[36] J. Ridky,[23] F. Riehn,[12,88] M. Risse,[50] V. Rizi,[22,11] E. Rodriguez,[8,31] G. Rodriguez Fernandez,[81] J. Rodriguez Rojo,[21] S. Rossoni,[55] M. Roth,[31] E. Roulet,[5] A.C. Rovero,[52] A. Saftoiu,[89] M. Saharan,[7] F. Salamida,[22,11] H. Salazar,[90] G. Salina,[81] P. Sampathkumar,[31] N. San Martin,[24] J.D. Sanabria Gomez,[84] F. Sánchez,[8] E.M. Santos,[91] E. Santos,[23] F. Sarazin,[24] R. Sarmento,[2] R. Sato,[21] P. Savina,[10,11] V. Scherini,[47,42] H. Schieler,[31] M. Schimassek,[57] M. Schimp,[71] D. Schmidt,[31] O. Scholten,[38,92] H. Schoorlemmer,[7,6] P. Schovánek,[23] F.G. Schröder,[68,31] J. Schulte,[36] T. Schulz,[23] S.J. Sciutto,[51] M. Scornavacche,[8,31] A. Sedoski,[8] A. Segreto,[93,14] S. Sehgal,[71] S.U. Shivashankara,[67] G. Sigl,[55] K. Simkova,[38,64] F. Simon,[63] R. Šmída,[69] P. Sommers,[94] R. Squartini,[43] M. Stadelmaier,[31,17,16] S. Stanič,[67] J. Stasielak,[34] P. Stassi,[25] S. Strähnz,[28] M. Straub,[36] T. Suomijärvi,[29] A.D. Supanitsky,[8] Z. Svozilikova,[23] K. Syrokvas,[83] Z. Szadkowski,[87] F. Tairli,[1] M. Tambone,[45,18] A. Tapia,[95] C. Taricco,[19,4] C. Timmermans,[6,7] O. Tkachenko,[23] P. Tobiska,[23] C.J. Todero Peixoto,[41] B. Tomé,[2] A. Travaini,[43] P. Travnicek,[23] M. Tueros,[51] M. Unger,[31] R. Uzeiroska,[71] L. Vaclavek,[44] M. Vacula,[44] I. Vaiman,[10,11] J.F. Valdés Galicia,[58] L. Valore,[45,18] P. van Dillen,[7,6] E. Varela,[90] V. Vašíčková,[71] A. Vásquez-Ramírez,[84] D. Veberič,[31] I.D. Vergara Quispe,[51] S. Verpoest,[68] V. Verzi,[81] J. Vicha,[23] J. Vink,[96] S. Vorobiov,[67] J.B. Vuta,[23] C. Watanabe,[48] A.A. Watson,[97] A. Weindl,[31] M. Weitz,[71] L. Wiencke,[24] H. Wilczyński,[34] B. Wundheiler,[8] B. Yue,[71] A. Yushkov,[23] E. Zas,[12] D. Zavrtanik,[67,66] and M. Zavrtanik[66,67]

(The Pierre Auger Collaboration)*

[1] *University of Adelaide, Adelaide, S.A., Australia*

[2] *Laboratório de Instrumentação e Física Experimental de Partículas – LIP and Instituto Superior Técnico – IST, Universidade de Lisboa – UL, Lisboa, Portugal*

[3]*Osservatorio Astrofisico di Torino (INAF), Torino, Italy*
[4]*INFN, Sezione di Torino, Torino, Italy*
[5]*Centro Atómico Bariloche and Instituto Balseiro (CNEA-UNCuyo-CONICET), San Carlos de Bariloche, Argentina*
[6]*Nationaal Instituut voor Kernfysica en Hoge Energie Fysica (NIKHEF), Science Park, Amsterdam, The Netherlands*
[7]*IMAPP, Radboud University Nijmegen, Nijmegen, The Netherlands*
[8]*Instituto de Tecnologías en Detección y Astropartículas (CNEA, CONICET, UNSAM), Buenos Aires, Argentina*
[9]*Universidad Tecnológica Nacional – Facultad Regional Buenos Aires, Buenos Aires, Argentina*
[10]*Gran Sasso Science Institute, L'Aquila, Italy*
[11]*INFN Laboratori Nazionali del Gran Sasso, Assergi (L'Aquila), Italy*
[12]*Instituto Galego de Física de Altas Enerxías (IGFAE),*
Universidade de Santiago de Compostela, Santiago de Compostela, Spain
[13]*Università di Catania, Dipartimento di Fisica e Astronomia "Ettore Majorana", Catania, Italy*
[14]*INFN, Sezione di Catania, Catania, Italy*
[15]*Department of Physics and Astronomy, Lehman College, City University of New York, Bronx, NY, USA*
[16]*Università di Milano, Dipartimento di Fisica, Milano, Italy*
[17]*INFN, Sezione di Milano, Milano, Italy*
[18]*INFN, Sezione di Napoli, Napoli, Italy*
[19]*Università Torino, Dipartimento di Fisica, Torino, Italy*
[20]*Universidad Michoacana de San Nicolás de Hidalgo, Morelia, Michoacán, México*
[21]*Observatorio Pierre Auger and Comisión Nacional de Energía Atómica, Malargüe, Argentina*
[22]*Università dell'Aquila, Dipartimento di Scienze Fisiche e Chimiche, L'Aquila, Italy*
[23]*Institute of Physics of the Czech Academy of Sciences, Prague, Czech Republic*
[24]*Colorado School of Mines, Golden, CO, USA*
[25]*Univ. Grenoble Alpes, CNRS, Grenoble Institute of Engineering Univ. Grenoble Alpes, LPSC-IN2P3, 38000 Grenoble, France*
[26]*Max-Planck-Institut für Radioastronomie, Bonn, Germany*
[27]*Instituto de Física de Rosario (IFIR) – CONICET/U.N.R. and Facultad de Ciencias Bioquímicas y Farmacéuticas U.N.R., Rosario, Argentina*
[28]*Karlsruhe Institute of Technology (KIT), Institute for Experimental Particle Physics, Karlsruhe, Germany*
[29]*Université Paris-Saclay, CNRS/IN2P3, IJCLab, Orsay, France*
[30]*Institut universitaire de France (IUF), France*
[31]*Karlsruhe Institute of Technology (KIT), Institute for Astroparticle Physics, Karlsruhe, Germany*
[32]*International Center of Advanced Studies and Instituto de Ciencias Físicas,*
ECyT-UNSAM and CONICET, Campus Miguelete – San Martín, Buenos Aires, Argentina
[33]*Universidade Estadual de Campinas (UNICAMP), IFGW, Campinas, SP, Brazil*
[34]*Institute of Nuclear Physics PAN, Krakow, Poland*
[35]*Colorado State University, Fort Collins, CO, USA*
[36]*RWTH Aachen University, III. Physikalisches Institut A, Aachen, Germany*
[37]*Universidad de Granada and C.A.F.P.E., Granada, Spain*
[38]*Vrije Universiteit Brussels, Brussels, Belgium*
[39]*Universidad Autónoma de Chiapas, Tuxtla Gutiérrez, Chiapas, México*
[40]*Instituto de Tecnologías en Detección y Astropartículas (CNEA, CONICET, UNSAM),*
and Universidad Tecnológica Nacional – Facultad Regional Mendoza (CONICET/CNEA), Mendoza, Argentina
[41]*Universidade de São Paulo, Escola de Engenharia de Lorena, Lorena, SP, Brazil*
[42]*INFN, Sezione di Lecce, Lecce, Italy*
[43]*Observatorio Pierre Auger, Malargüe, Argentina*
[44]*Palacky University, Olomouc, Czech Republic*
[45]*Università di Napoli "Federico II", Dipartimento di Fisica "Ettore Pancini", Napoli, Italy*
[46]*Politecnico di Milano, Dipartimento di Scienze e Tecnologie Aerospaziali , Milano, Italy*
[47]*Università del Salento, Dipartimento di Matematica e Fisica "E. De Giorgi", Lecce, Italy*
[48]*Universidade Federal do Rio de Janeiro, Instituto de Física, Rio de Janeiro, RJ, Brazil*
[49]*Case Western Reserve University, Cleveland, OH, USA*
[50]*Universität Siegen, Department Physik – Experimentelle Teilchenphysik, Siegen, Germany*
[51]*IFLP, Universidad Nacional de La Plata and CONICET, La Plata, Argentina*
[52]*Instituto de Astronomía y Física del Espacio (IAFE, CONICET-UBA), Buenos Aires, Argentina*
[53]*Departamento de Física and Departamento de Ciencias de la Atmósfera y los Océanos,*
FCEyN, Universidad de Buenos Aires and CONICET, Buenos Aires, Argentina
[54]*Instituto Federal de Educação, Ciência e Tecnologia do Rio de Janeiro (IFRJ), Brazil*
[55]*Universität Hamburg, II. Institut für Theoretische Physik, Hamburg, Germany*
[56]*Universidade de São Paulo, Instituto de Física de São Carlos, São Carlos, SP, Brazil*
[57]*CNRS/IN2P3, IJCLab, Université Paris-Saclay, Orsay, France*
[58]*Universidad Nacional Autónoma de México, México, D.F., México*
[59]*Centro Brasileiro de Pesquisas Fisicas, Rio de Janeiro, RJ, Brazil*
[60]*Universidade Federal do Paraná, Setor Palotina, Palotina, Brazil*
[61]*Stichting Astronomisch Onderzoek in Nederland (ASTRON), Dwingeloo, The Netherlands*
[62]*New York University, New York, NY, USA*

[63] Karlsruhe Institute of Technology (KIT), Institut für Prozessdatenverarbeitung und Elektronik, Karlsruhe, Germany
[64] Université Libre de Bruxelles (ULB), Brussels, Belgium
[65] Michigan Technological University, Houghton, MI, USA
[66] Experimental Particle Physics Department, J. Stefan Institute, Ljubljana, Slovenia
[67] Center for Astrophysics and Cosmology (CAC), University of Nova Gorica, Nova Gorica, Slovenia
[68] University of Delaware, Department of Physics and Astronomy, Bartol Research Institute, Newark, DE, USA
[69] University of Chicago, Enrico Fermi Institute, Chicago, IL, USA
[70] now at Graduate School of Science, Osaka Metropolitan University, Osaka, Japan
[71] Bergische Universität Wuppertal, Department of Physics, Wuppertal, Germany
[72] Universidade Estadual de Feira de Santana, Feira de Santana, Brazil
[73] Fermi National Accelerator Laboratory, Fermilab, Batavia, IL, USA
[74] Institute of Space Science, Bucharest-Magurele, Romania
[75] Centro Federal de Educação Tecnológica Celso Suckow da Fonseca, Petropolis, Brazil
[76] Universidade Federal do ABC, Santo André, SP, Brazil
[77] Laboratoire de Physique Nucléaire et de Hautes Energies (LPNHE),
Sorbonne Université, Université de Paris, CNRS-IN2P3, Paris, France
[78] Università di Palermo, Dipartimento di Fisica e Chimica "E. Segrè", Palermo, Italy
[79] Louisiana State University, Baton Rouge, LA, USA
[80] Università di Roma "Tor Vergata", Dipartimento di Fisica, Roma, Italy
[81] INFN, Sezione di Roma "Tor Vergata", Roma, Italy
[82] Laboratorio Atmósfera – Departamento de Investigaciones en Láseres y sus Aplicaciones – UNIDEF (CITEDEF-CONICET), Argentina
[83] Charles University, Faculty of Mathematics and Physics,
Institute of Particle and Nuclear Physics, Prague, Czech Republic
[84] Universidad Industrial de Santander, Bucaramanga, Colombia
[85] Unidad Profesional Interdisciplinaria en Ingeniería y Tecnologías Avanzadas
del Instituto Politécnico Nacional (UPIITA-IPN), México, D.F., México
[86] Universidade Federal de Campina Grande, Centro de Ciencias e Tecnologia, Campina Grande, Brazil
[87] University of Lódź, Faculty of High-Energy Astrophysics,Lódź, Poland
[88] now at Technische Universität Dortmund and Ruhr-Universität Bochum, Dortmund and Bochum, Germany
[89] "Horia Hulubei" National Institute for Physics and Nuclear Engineering, Bucharest-Magurele, Romania
[90] Benemérita Universidad Autónoma de Puebla, Puebla, México
[91] Universidade de São Paulo, Instituto de Física, São Paulo, SP, Brazil
[92] also at Kapteyn Institute, University of Groningen, Groningen, The Netherlands
[93] Istituto di Astrofisica Spaziale e Fisica Cosmica di Palermo (INAF), Palermo, Italy
[94] Pennsylvania State University, University Park, PA, USA
[95] Universidad de Medellín, Medellín, Colombia
[96] Universiteit van Amsterdam, Faculty of Science, Amsterdam, The Netherlands
[97] School of Physics and Astronomy, University of Leeds, Leeds, United Kingdom

(Dated: October 30, 2025)

The energy spectrum of cosmic rays above 2.5 EeV has been measured across the declination range $-90^\circ \le \delta \le +44.8^\circ$ using $\sim$ 310,000 events accrued at the Pierre Auger Observatory from an exposure of $(104{,}900 \pm 3{,}100)$ km^2 sr yr. No significant variations of energy spectra with declination are observed, after allowing or not for non-uniformities across the sky arising from the well-established dipolar anisotropies in the arrival directions of ultra-high energy cosmic rays. The instep feature in the spectrum at $\simeq$ 10 EeV reported previously is now established at a significance above $5\,\sigma$. Within the statistics, the energy spectra are indistinguishable across declinations so disfavoring an origin for the instep from a few distinctive sources.

I. INTRODUCTION

The discovery at the Pierre Auger Observatory [1] of a dipole in the distribution of cosmic rays of energy above 8 EeV of amplitude $\sim 6\%$ at a significance of over $5\,\sigma$ marks a significant advance in the field of high-energy cosmic-ray astronomy [2]. The status of this result is now $6.8\,\sigma$, with an increase of the dipole amplitude with energy identified [3]. Above 32 EeV, associations of high-energy cosmic rays with an overdensity in the Centaurus region, and with starburst galaxies, have been found, but only at the $4\,\sigma$ level [4]. Beyond 100 EeV, the arrival direction distribution across the whole sky, derived from a combination of data from the Auger Observatory and the Telescope Array, is featureless [5]. It is thus important to examine whether the energy spectrum varies with declination, particularly at the highest energies, where the new spectral feature near 10 EeV, identified in data from the Auger Observatory [6], indicates a two-step suppression of the spectrum [7, 8]. An analysis of spectra in bands of declination is presented, exploiting the 1.2 m deep-water Cherenkov detectors of the Auger Observatory to obtain measurements over declinations -90° to $+44.8^\circ$.

At large zenith angles θ, the effects of the geomagnetic field on the distribution of the muons in air showers increases so that

* spokespersons@auger.org; http://www.auger.org

the near-circular symmetry of signals around the shower axis found at low zenith angles is destroyed: above 70°, eccentricities over 0.9 are found. Accordingly, different methods of analyses are necessary for "vertical showers" ($\theta \leq 60°$) and for the more "inclined events" (60° to 80°). The procedures for dealing with events with $\theta \leq 60°$ are classical [9, 10]. Techniques to reconstruct events where the geomagnetic field is important were developed more recently [11], with the methods later adapted for use with data from the Auger Observatory. The procedure to obtain the energy of the primary particle for vertical showers is based on the determination of the signal in the water-Cherenkov detectors, $S(1000)$, interpolated at 1000 m from the centre of the shower [12], while for inclined events a parameter based on the number of muons in the shower, N_{19}, has been adopted [13, 14]. $S(1000)$ and N_{19} are subsequently converted into size parameters S_{38} and N_{68}, independent of the zenith angle, using the constant intensity method [6, 15]. Calorimetric estimates of primary energies are derived by calibrating these size parameters using fluorescence measurements, obtained on clear, moonless nights. Derivation of the energy spectrum from vertical events requires no assumptions about features of hadronic interactions at high energies or of the mass of the primary cosmic rays, apart from a 1.5% systematic uncertainty in the estimation of the invisible energy [6, 16]. Minimal assumptions about these parameters are required for the inclined events [17, 18]. Data used here were recorded between 1 January 2004 and 31 December 2022. For vertical events the exposure was $\mathcal{E}_{[0-60°]} = (81{,}100 \pm 2{,}400)$ km^2 sr yr, with 279,131 events recorded above 2.5 EeV, while for inclined showers 31,543 events above 4 EeV were recorded in an exposure of $\mathcal{E}_{[60°-80°]} = (23{,}800 \pm 700)$ km^2 sr yr. Exposures are independent of energy above these thresholds [6, 17], which are non-identical mainly due to the attenuation of the electromagnetic cascade at high zenith angles.

II. COMBINATION OF INDIVIDUAL SPECTRA

Given the latitude of the Observatory, $\lambda \simeq -35.2°$ and the zenith angle ranges mentioned in the previous section, the S_{38}-based dataset covers the range of declinations $-90° \leq \delta \leq +24.8°$ in equatorial coordinates, whereas the N_{68} one covers $-84.8° \leq \delta \leq +44.8°$. Our aim is to measure the spectrum over the whole declination range covered with the surface array, $-90° \leq \delta \leq +44.8°$. Thus the independent spectra from the S_{38}- and N_{68}-based analyses, shown as the circles and squares respectively in the top panel of Fig. 1, must be combined.

The combination procedure follows from that in [19]. The combined spectrum is obtained by forward-folding the effects of the finite energy accuracy of the detector into a proposed function tailored to describe a series of power-law falloffs,

$$J(E;\mathbf{p}) = J_0 \left(\frac{E}{E_0}\right)^{-\gamma_0} \frac{\prod_{j=1}^{3} \left[1 + \left(\frac{E}{E_{jk}}\right)^{\omega_{jk}^{-1}}\right]^{(\gamma_j-\gamma_k)\omega_{jk}}}{\prod_{j=1}^{3} \left[1 + \left(\frac{E_0}{E_{jk}}\right)^{\omega_{jk}^{-1}}\right]^{(\gamma_j-\gamma_k)\omega_{jk}}}, \quad (1)$$

with $k = j + 1$ and eight free parameters encompassed in $\mathbf{p}$,

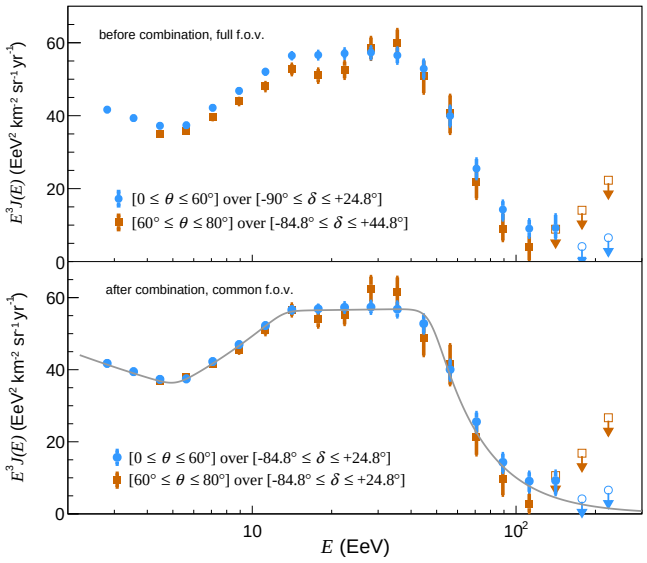


Figure 1. Individual energy spectra scaled by E^3 inferred from S_{38}- and N_{68}-based analyses before (top panel) and after (bottom panel) correcting the energies of inclined events to a best-fit common energy scale. The declination range after combination is reduced to $[-84.8°, +24.8°]$ to guarantee observation of the same sky. Upper limits at 90% confidence level are shown in empty bins. The gray line is the best-fit to data points after combination.

namely the overall normalization J_0, four spectral indices $(\gamma_0, \gamma_1, \gamma_2, \gamma_3)$ and three energy turning points E_{jk}; the parameters ω_{jk} that govern the width of the transition from γ_j to γ_k are fixed to $\omega_{jk} = 0.05$ [6]; the pivot energy is chosen as $E_0 = 10^{0.5}$ EeV. The parameters $\mathbf{p}$ are adjusted to obtain the best match between the observed number of events n_i in each differential energy bin of width $\Delta \log_{10} E = 0.1$ and the expected ones $\nu_i(\mathbf{p})$ simultaneously for both data streams. The minimization procedure is based on the product of Poissonian likelihood functions pertaining to each individual spectrum, $\mathcal{L}_{[0-60°]}$ and $\mathcal{L}_{[60°-80°]}$.

Both individual spectra are subject to systematic uncertainties, with contributions from the absolute energy scale (14%) [20], the exposure (3%) [21], the unfolding procedure ($\leq 2\%$) [6] and the energies inferred from S_{38} and N_{68} ($\leq 3\%$) [6, 14]. No indication of further systematics has been found from a comparison of spectra calculated over different time periods, seasons and ranges of zenith angle.

The systematic uncertainties relating to each S_{38}- and N_{68}-based analysis are common to both: the important exception concerns those inherited from the energy-calibration procedure that are uncorrelated as the two datasets used for calibration are independent. The largest uncertainties are related to the calibration of N_{68}, as it is based on 605 events compared to 4,703 for S_{38}. The statistics is limited by the high-quality criteria used to guarantee an accurate energy estimation with the fluorescence technique, and by the effective area for observing the maximum of shower development that drops rapidly with zenith angle [22, 23]. Therefore, our strategy for the combination is to correct the energies of the N_{68}-based dataset,

originally determined as $E = AN_{68}{}^{B}$, to a best-fit common energy scale, using two absolute departure parameters δA and δB such that $E' = (A+\delta A)N_{68}{}^{B+\delta B}$. As shown below, considering the uncertainties in N_{68} alone, the most significant ones, will suffice to obtain a satisfactory goodness-of-fit. Including those in S_{38} would improve further the combination, but is unnecessary.

In addition, as explained in the End Matter, the energy calibration of N_{68} may be affected by (logarithmic) non-linearities above ~ 10 EeV due to the sensitivity of N_{68} to the small, yet sharp, changes in mass composition recently uncovered [24, 25] and to experimental effects. A third departure parameter, δC, is therefore introduced so that the correction reads $E'' = (A+\delta A)N_{68}{}^{B+\delta B+\delta C}$ above 10 EeV.

During each step of the fit, the energy-bin boundaries of the N_{68}-based analysis are corrected by varying the extra-parameters $\mathbf{x} = (\delta A, \delta B, \delta C)$ that govern the uncorrelated systematic uncertainties. Correspondingly, an extra-term in the joint likelihood restricts the values of the extra-parameters within their uncertainties. It is constructed by considering on the one hand the sum of two random variables δB and δC, and on the other hand the correlation between δA and δB. The log-likelihood function therefore stems from the convolution of a 2D Gaussian with correlation parameter $\rho \simeq -0.66$ with a 1D Gaussian pertaining to δC alone,

$$-2\ln\mathcal{L}_{\mathbf{x}}(\delta A,\delta B,\delta C) = \frac{\delta A^2(\sigma_B^2+\sigma_C^2) - 2\rho\delta A\delta B\sigma_A\sigma_B + (\delta B+\delta C)^2\sigma_A^2}{\sigma_A^2(\sigma_C^2+\sigma_B^2(1-\rho^2))}, \quad (2)$$

with $\sigma_A \simeq 6\times10^{-2}$ EeV, $\sigma_B = 1.4\times10^{-2}$ and, as shown in the End Matter, $\sigma_C = 3\times10^{-2}$ from the systematic uncertainties in N_{68} and in the relationship between N_{68} and energy.

In this way, for unrealistic changes in $(\delta A, \delta B, \delta C)$, the $-2\ln\mathcal{L}_{\mathbf{x}}(\delta A,\delta B,\delta C)$ term acts as a penalty factor while minimizing the total log-likelihood function $-2\ln\mathcal{L}(\mathbf{p},\mathbf{x})$, which, overall, reads as

$$\mathcal{L}(\mathbf{p},\mathbf{x}) = \mathcal{L}_{[0-60^\circ]}(\mathbf{p},\mathbf{x}) \times \mathcal{L}_{[60^\circ-80^\circ]}(\mathbf{p},\mathbf{x}) \times \mathcal{L}_{\mathbf{x}}(\mathbf{x}). \quad (3)$$

The outcome of the forward-folding is the set of parameters $\mathbf{p}$, and $\mathbf{x}$, that allows calculation of ν_i and μ_i, which are the expected number of events including and not including the detector effects, respectively. Unfolding factors, defined as $c_i = \mu_i/\nu_i$, are then applied to correct for bin-to-bin migration induced by the finite accuracy of the response functions, which are determined in a data-driven manner [6] and given in the Supplemental material. The resulting spectral point for each bin is obtained as

$$J_i = \frac{c_i n_{i[0-60^\circ]} + c_i n_{i[60^\circ-80^\circ]}}{\mathcal{E}_i \Delta E_i}, \quad (4)$$

with $\mathcal{E}_i = \mathcal{E}_{[0-60^\circ]}$ for $0.4 \le \log_{10}(E/\mathrm{EeV}) \le 0.6$ and $\mathcal{E}_i = \mathcal{E}_{[0-60^\circ]} + \mathcal{E}_{[60^\circ-80^\circ]}$ for $\log_{10}(E/\mathrm{EeV}) \ge 0.6$. The minimization procedure, applied only to the events in the declination band $[-84.8^\circ, +24.8^\circ]$, common to both datasets, to guarantee observation of the same sky so that spectra must be in statistical agreement, yields values of $\delta A/A \simeq (3.0\pm0.6)\%$, $\delta B/B \simeq (0.3\pm1.5)\%$, respectively corresponding to shifts of 2.6 σ_A and 0.2 σ_B, and $\delta C \simeq (-2.0\pm2.0)\times10^{-2}$. The resulting spectra are displayed in the lower panel of Fig. 1. The most significant changes are in the lower energy bins, where the statistical power is greatest. Note that, as the analysis is designed so that $\mathcal{L}_{[0-60^\circ]}(\mathbf{p},\mathbf{x})$ is independent of $\mathbf{x}$, the changes impact dominantly the N_{68}-based spectrum. The combined spectrum obtained with eqn. 4 shows a deviance of $D = 40.5$, which, if considered to follow a "C statistics" [26], can be compared to the expectation of $\langle D\rangle = 26.9\pm7.0$ to yield a p-value of $\simeq 0.12$.

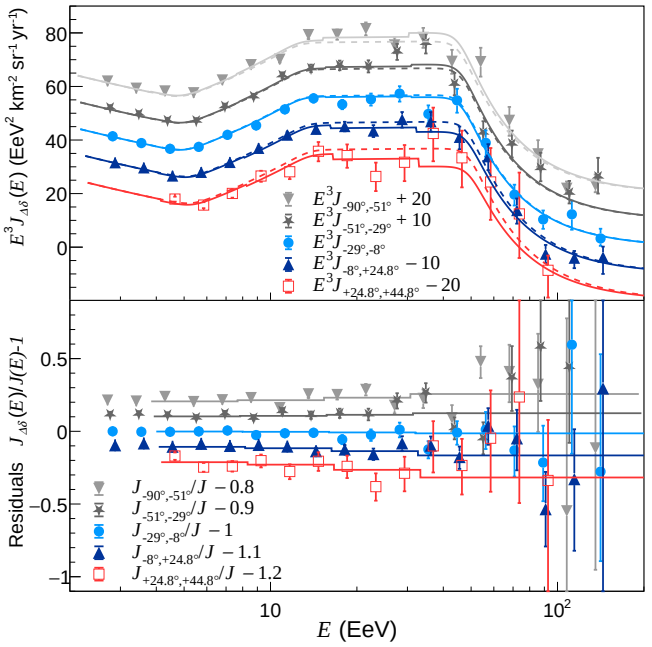


Figure 2. Top: Energy spectra in five declination ranges. The dotted reference lines are the best-fit function for the spectrum combined over $[-84.8^\circ, +24.8^\circ]$; the full lines account for the impact of dipole anisotropies in each band. Bottom: Corresponding residuals. Artificial shifts are applied for visualization purpose. An alternative view of the residuals is provided in the Supplemental material.

III. SEARCHES FOR DECLINATION DEPENDENCES

The best-fit parameters for $(\delta A, \delta B, \delta C)$ that yield statistical agreement of spectra in the declination range $[-84.8^\circ, +24.8^\circ]$ are used to search for declination dependences in five ranges over $[-90^\circ, +44.8^\circ]$. The first range corresponds to the most northerly declination band $[+24.8^\circ, +44.8^\circ]$: it is selected as it only contains inclined events (5,632 after energy corrections for an exposure of $(4{,}100\pm120)$ km^2 sr yr) and it is thus not considered in the combination fit. The remaining portion of the sky $[-90^\circ, +24.8^\circ]$ is divided in four declination ranges with exposures similar to within 1% and averaging 25,000 km^2 sr yr. Detailed comparisons of the spectra in the five declination bands are shown in Fig. 2. In the top panel, individual spectra are compared with the best-fit function (dotted lines) for the

Table I. Spectral parameters $\mathbf{p}$ in several declination bands: normalization J_0 in $\mathrm{km^{-2}\,sr^{-1}\,yr^{-1}\,EeV^{-1}}$ units, indices γ_j and break energies E_{jk} in EeV units; and probabilities $P(\geq Q^2)$ that $\mathbf{p}_{\Delta\delta}$ departs from $\mathbf{p}_{\rm ref}$ measured across $[-84.8^\circ, +24.8^\circ]$. In the declination band $[+24.8^\circ, +44.8^\circ]$, the threshold of the N_{68}-based analysis does not allow for measuring γ_1 and E_{12}, which are fixed to their value found across $[-84.8^\circ, +24.8^\circ]$.

$[\delta_{\rm min}, \delta_{\rm max}]$	J_0	γ_1	γ_2	γ_3	γ_4	E_{12}	E_{23}	E_{34}	$P(\geq Q^2)$
$[-84.8^\circ, +24.8^\circ]$	1.271 ± 0.004	3.26 ± 0.01	2.51 ± 0.03	2.99 ± 0.03	5.3 ± 0.2	5.1 ± 0.1	13 ± 1	48 ± 2	–
$[-90^\circ, -51^\circ]$	1.278 ± 0.007	3.24 ± 0.02	2.54 ± 0.06	3.18 ± 0.06	7.2 ± 1.0	5.1 ± 0.2	17 ± 2	62 ± 4	23%
$[-51^\circ, -29^\circ]$	1.281 ± 0.007	3.26 ± 0.02	2.46 ± 0.06	2.87 ± 0.06	4.6 ± 0.4	5.2 ± 0.2	12 ± 2	39 ± 4	13%
$[-29^\circ, -8^\circ]$	1.257 ± 0.007	3.28 ± 0.02	2.54 ± 0.06	3.02 ± 0.06	5.6 ± 0.4	4.9 ± 0.2	13 ± 2	49 ± 4	71%
$[-8^\circ, +24.8^\circ]$	1.266 ± 0.007	3.26 ± 0.02	2.50 ± 0.06	2.97 ± 0.06	6.1 ± 0.4	5.1 ± 0.2	12 ± 2	51 ± 4	34%
$[+24.8^\circ, +44.8^\circ]$	1.26 ± 0.03	3.26 (fixed)	2.6 ± 0.2	3.0 ± 0.2	11 ± 10	5.1 (fixed)	13 ± 4	69 ± 20	53%

spectrum combined over $[-84.8^\circ, +24.8^\circ]$ and with the same best-fit function (full lines) taking into account the variation of the dipole amplitude with energy and declination measured above 4 EeV. Because the energy-spectrum estimator is based primarily on the observed number of events through the directional exposure function $\omega(\delta)$, the expression of $J_{\Delta\delta}(E;\mathbf{p})$ is obtained as [6],

$$J_{\Delta\delta}(E;\mathbf{p}) = J(E;\mathbf{p})\left(1+ \frac{\mathcal{E}_0}{\mathcal{E}_{\Delta\delta}} \frac{\int_{\Delta\delta} \mathrm{d}\delta \cos\delta\, \omega(\delta) + d_z(E) \int_{\Delta\delta} \mathrm{d}\delta \cos\delta \sin\delta\, \omega(\delta)}{\int \mathrm{d}\delta \cos\delta\, \omega(\delta) + d_z(E) \int \mathrm{d}\delta \cos\delta \sin\delta\, \omega(\delta)}\right), \quad (5)$$

with $\mathcal{E}_0$ the total exposure over the declination range of reference $[-84.8^\circ, +24.8^\circ]$, $\mathcal{E}_{\Delta\delta}$ that over the declination band under consideration, and where the integrations in the denominator are carried out over $[-84.8^\circ, +24.8^\circ]$. The coefficients $d_z(E)$ read $\{-0.013, -0.031, -0.070\}$ in differential bins of width $\Delta \log_{10} E = 0.3$ between 4 and 32 EeV and -0.13 above 32 EeV [3]. In the bottom panel, the best-fit function over $[-84.8^\circ, +24.8^\circ]$ is taken as a reference and the residual differences from this spectrum are compared with expectations. The residuals follow the trend imprinted by the dipole between 4 and 32 EeV; statistical fluctuations dominate above 32 EeV.

Spectral parameters for each declination band, $\mathbf{p}_{\Delta\delta}$, are obtained by applying the combination procedure, except in the northernmost band where only inclined events contribute: they are listed in Table I. A quantitative statement on the statistical agreement between $\mathbf{p}_{\Delta\delta}$ and the reference parameters across $[-84.8^\circ, +24.8^\circ]$, $\mathbf{p}_{\rm ref}$, can be drawn from the distance-squared quantity

$$Q^2 = (\mathbf{p}_{\Delta\delta} - \mathbf{p}_{\rm ref})^{\rm T} (\mathbf{\Sigma}_{\Delta\delta} + \mathbf{\Sigma}_{\rm ref})^{-1} (\mathbf{p}_{\Delta\delta} - \mathbf{p}_{\rm ref}), \quad (6)$$

which accounts for the correlations between parameters through their respective covariance matrices $\mathbf{\Sigma}_{\Delta\delta}$ and $\mathbf{\Sigma}_{\rm ref}$ given in the Supplemental material. Some fraction of the uncertainty in the exposure may depend on the declination [27]. The array is slightly tilted by $\simeq 0.2^\circ$ in the southeastern direction $\varphi_{\rm tilt} \simeq -30^\circ$. Besides, the latitude of the Observatory varies by $\simeq 0.5^\circ$ between detectors located in the northernmost and southernmost positions. Considering the uncertainties in the determination of $\varphi_{\rm tilt}$ and the impact of the spatial extension of the array, we conservatively allocate an uncertainty of 100 $\mathrm{km^2\,sr\,yr}$ in the exposure of each declination band that propagates into an additional contribution to the uncertainty in J_0. The probability that the set of parameters $\mathbf{p}_{\Delta\delta}$ departs from the reference ones is obtained by drawing at random mock samples and by counting the fraction of them displaying a value Q^2 larger than that in data. No significant departure is observed.

Some departure in γ_3, E_{34} and γ_4, which shape the spectrum at the highest energies, are evident in the band $[-51^\circ, -29^\circ]$. The departure remains quasi-identical when fixing the other parameters to their values in the band $[-84.8^\circ, +24.8^\circ]$. This declination range encompasses the Centaurus region in which an overdensity over a circular region of $\simeq 24^\circ$ is present [4] and which has attracted attention in, e.g., [28–33]. We have estimated the spectral features by restricting further, within the declination band, the region of interest within $\simeq 24^\circ$ around the position (right ascension $\alpha = 201^\circ$, declination $\delta = -43^\circ$) to check whether the harder values of γ_3 and γ_4 as well as the smaller value of E_{34} elsewhere can be attributed to the overdensity. However, statistical fluctuations prevent drawing any conclusion, given that $\gamma_3 = 2.8 \pm 0.3$, $E_{34} = (67 \pm 11)$ EeV and $\gamma_4 = 9 \pm 4$ in that specific region. In parallel, the values obtained by excluding the 24° window around the Centaurus region from the declination band are $\gamma_3 = 2.88 \pm 0.07$, $E_{34} = (37 \pm 4)$ EeV and $\gamma_4 = 4.5 \pm 0.5$, close to those observed over the whole $[-51^\circ : -29^\circ]$ band. The same outcome holds about other, more modest, overdensities over the same scale that have attracted attention [30, 32, 34, 35]: $\gamma_3 = 2.9 \pm 0.2$, $E_{34} = (41 \pm 11)$ EeV and $\gamma_4 = 5 \pm 1$ around the region of NGC 253 ($\alpha = 11.9^\circ, \delta = -25.3^\circ$), and, within the declination band $[-8^\circ, +24.8^\circ]$, $\gamma_3 = 3.3 \pm 0.3$, $E_{34} = (58 \pm 18)$ EeV and $\gamma_4 = 5 \pm 1$ around the region of NGC 1068 galaxy ($\alpha = 40.5^\circ, \delta = 0^\circ$). Finally, since the northernmost declination band is also observed using Telescope Array with an exposure $\simeq 20\%$ larger [36], it is interesting to note that the spectral parameters do not show deviations with respect to those of the $[-84.8^\circ, +24.8^\circ]$ band.

We conclude, consistent with large-scale anisotropy measurements [3] and with our previous report from an exposure of 60,400 $\mathrm{km^2\,sr\,yr}$ and covering declinations from -90° to $+24.8^\circ$ [7], that the energy spectra are identical to within a mild dipolar modulation with declination from -90° to $+44.8^\circ$.

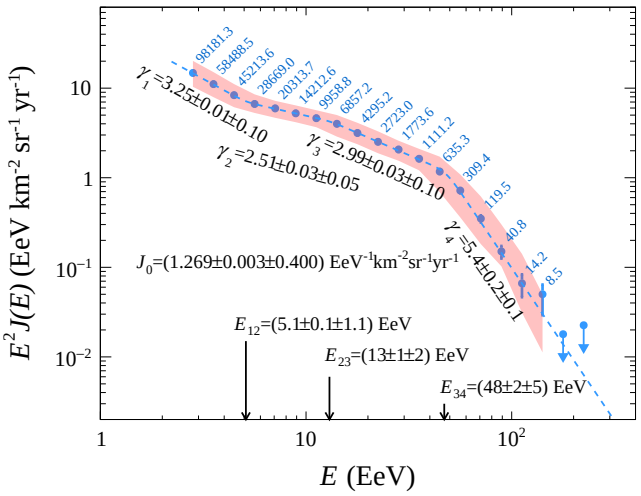


Figure 3. Energy spectrum scaled by E^2 (energy flux) across declinations $[-90°, +44.8°]$. The number of events corrected for detector effects is indicated in each bin. The red band stands for the systematic uncertainties while the dotted line indicates the best-fit function described by the spectral features given with their statistical and systematic uncertainties.

IV. SPECTRUM ACROSS DECLINATIONS −90° TO +44.8°

Given the statistical agreement of the spectra across declinations, we present in Fig. 3 the combined spectrum across declinations −90° to +44.8°, scaled by E^2 (energy flux). The colored band shows the systematic uncertainties, which have been propagated by repeating the analysis on datasets obtained by randomly sampling the different sources of systematics that affect individual energies and exposure. The main contribution stems, by far, from the 14% uncertainty in energy scale. The various spectral features, with their statistical and systematic uncertainties, are given in Fig. 3. The data, included those in each declination band, are listed on a point-by-point basis in the Supplemental material.

Beyond the well-known features of the ankle and the steepening, earlier evidence for "instep" [6] is reinforced with this measurement. We had previously disfavored, with 3.9 σ confidence, a model of the energy spectrum consisting of a series of two power laws followed by a slow suppression [6]. By drawing at random mock samples of observed energies following this reference model without instep, and by reconstructing the corresponding spectra using the reference model and the alternative one (eqn. 1), we built the distribution of the test statistics t from the ratio of the likelihood values associated with each hypothesis. Only two out of 10^8 realizations show a test statistic greater than the observed one ($t \simeq 38$). Thus for 1-sided Gaussian distributions, the reference model can be rejected at the 5.5 σ confidence level. The significance remains above 5.5 σ when the complete chain of analysis is repeated with the energy scale adjusted by ±14% (the dominant systematic uncertainty) from the nominal one.

V. DISCUSSION

The first measurement of the energy spectrum of cosmic rays over the entire range of declination covered by the surface array of the Pierre Auger Observatory with an exposure of 104,900 km^2 sr yr has been presented. This is made possible by using independent spectra measured over $[0, 60°]$ and $[60°, 80°]$ combined through a forward-folding procedure that makes use of a unique function to describe the underlying spectrum. Statistical agreement is obtained by increasing the energies inferred from N_{68} values measured between 60° and 80° from +2.9% at 4 EeV to 3.1% at 10 EeV; the increase then slows and energies are changed by −1% at 100 EeV. Such changes are consistent with the uncertainties in the energy assignments to N_{68}.

A search for a declination dependence was performed by comparing the energy spectrum in five declination ranges with that measured in the band $[-84.8°, +24.8°]$, which is covered when measuring individual spectra between $[0, 60°]$ and $[60°, 80°]$ in zenith angle. All spectra are found to be consistent with the reference one, apart from the mild modulation expected from a dipolar anisotropy previously uncovered [3]. Notably this statement applies to the northernmost declination band $[+24.8°, +44.8°]$, where only inclined events are available.

The combination of the two individual measurements and the statistical agreement across declinations lead to the construction of the spectrum across −90° to +44.8° declinations, where the features of the ankle, the instep and the suppression are firmly established. Among those features, the significance of the instep, originally uncovered with 3.9 σ confidence [6], has reached 5.5 σ. The increase in significance is consistent with the increase in exposure, in particular from the inclined events.

The absence of declination dependencies disfavors that the origin of the instep feature may be attributed to the distinctive spectrum of a small number of foreground sources contributing significantly to the total intensity. By contrast, the steepening seems to reflect the interplay between the flux contributions of the helium and carbon-nitrogen-oxygen components from rather similar sources [7, 37]. This is inline with the narrow range of maximum rigidity at the sources that can be inferred from the succession of rather pure-composition components of nuclei above 10 EeV [38–40]. The improved sensitivity in mass-composition with the upgraded Observatory [41] will allow further characterization on the instep thus shedding more light on its origin.

Acknowledgments. The successful installation, commissioning, and operation of the Pierre Auger Observatory would not have been possible without the strong commitment and effort from the technical and administrative staff in Malargüe. We are very grateful to the following agencies and organizations for financial support:

Argentina – Comisión Nacional de Energía Atómica; Agencia Nacional de Promoción Científica y Tecnológica (ANPCyT); Consejo Nacional de Investigaciones Científicas y Técnicas (CONICET); Gobierno de la Provincia de Mendoza; Municipalidad de Malargüe; NDM Holdings and Valle Las

Leñas; in gratitude for their continuing cooperation over land access; Australia – the Australian Research Council; Belgium – Fonds de la Recherche Scientifique (FNRS); Research Foundation Flanders (FWO), Marie Curie Action of the European Union Grant No. 101107047; Brazil – Conselho Nacional de Desenvolvimento Científico e Tecnológico (CNPq); Financiadora de Estudos e Projetos (FINEP); Fundação de Amparo à Pesquisa do Estado de Rio de Janeiro (FAPERJ); São Paulo Research Foundation (FAPESP) Grants No. 2019/10151-2, No. 2010/07359-6 and No. 1999/05404-3; Ministério da Ciência, Tecnologia, Inovações e Comunicações (MCTIC); Czech Republic – GACR 24-13049S, CAS LQ100102401, MEYS LM2023032, CZ.02.1.01/0.0/0.0/16_013/0001402, CZ.02.1.01/0.0/0.0/18_046/0016010 and CZ.02.1.01/0.0/0.0/17_049/0008422 and CZ.02.01.01/00/22_008/0004632; France – Centre de Calcul IN2P3/CNRS; Centre National de la Recherche Scientifique (CNRS); Conseil Régional Ile-de-France; Département Physique Nucléaire et Corpusculaire (PNC-IN2P3/CNRS); Département Sciences de l'Univers (SDU-INSU/CNRS); Institut Lagrange de Paris (ILP) Grant No. LABEX ANR-10-LABX-63 within the Investissements d'Avenir Programme Grant No. ANR-11-IDEX-0004-02; Germany – Bundesministerium für Bildung und Forschung (BMBF); Deutsche Forschungsgemeinschaft (DFG); Finanzministerium Baden-Württemberg; Helmholtz Alliance for Astroparticle Physics (HAP); Helmholtz-Gemeinschaft Deutscher Forschungszentren (HGF); Ministerium für Kultur und Wissenschaft des Landes Nordrhein-Westfalen; Ministerium für Wissenschaft, Forschung und Kunst des Landes Baden-Württemberg; Italy – Istituto Nazionale di Fisica Nucleare (INFN); Istituto Nazionale di Astrofisica (INAF); Ministero dell'Università e della Ricerca (MUR); CETEMPS Center of Excellence; Ministero degli Affari Esteri (MAE), ICSC Centro Nazionale di Ricerca in High Performance Computing, Big Data and Quantum Computing, funded by European Union NextGenerationEU, reference code CN_00000013; México – Consejo Nacional de Ciencia y Tecnología (CONACYT) No. 167733; Universidad Nacional Autónoma de México (UNAM); PAPIIT DGAPA-UNAM; The Netherlands – Ministry of Education, Culture and Science; Netherlands Organisation for Scientific Research (NWO); Dutch national e-infrastructure with the support of SURF Cooperative; Poland – Ministry of Education and Science, grants No. DIR/WK/2018/11 and 2022/WK/12; National Science Centre, grants No. 2016/22/M/ST9/00198, 2016/23/B/ST9/01635, 2020/39/B/ST9/01398, and 2022/45/B/ST9/02163; Portugal – Portuguese national funds and FEDER funds within Programa Operacional Factores de Competitividade through Fundação para a Ciência e a Tecnologia (COMPETE); Romania – Ministry of Research, Innovation and Digitization, CNCS-UEFISCDI, contract no. 30N/2023 under Romanian National Core Program LAPLAS VII, grant no. PN 23 21 01 02 and project number PN-III-P1-1.1-TE-2021-0924/TE57/2022, within PNCDI III; Slovenia – Slovenian Research Agency, grants P1-0031, P1-0385, I0-0033, N1-0111; Spain – Ministerio de Ciencia e Innovación/Agencia Estatal de Investigación (PID2019-105544GB-I00, PID2022-140510NB-I00 and RYC2019-027017-I), Xunta de Galicia (CIGUS Network of Research Centers, Consolidación 2021 GRC GI-2033, ED431C-2021/22 and ED431F-2022/15), Junta de Andalucía (SOMM17/6104/UGR and P18-FR-4314), and the European Union (Marie Sklodowska-Curie 101065027 and ERDF); USA – Department of Energy, Contracts No. DE-AC02-07CH11359, No. DE-FR02-04ER41300, No. DE-FG02-99ER41107 and No. DE-SC0011689; National Science Foundation, Grant No. 0450696, and NSF-2013199; The Grainger Foundation; Marie Curie-IRSES/EPLANET; European Particle Physics Latin American Network; and UNESCO.

[1] A. Aab et al. (Pierre Auger), Nucl. Instrum. Meth. A **798**, 172 (2015), arXiv:1502.01323 [astro-ph.IM].
[2] A. Aab et al. (Pierre Auger), Science **357**, 1266 (2017), arXiv:1709.07321 [astro-ph.HE].
[3] A. A. Halim et al. (Pierre Auger), Astrophys. J. **976**, 48 (2024), arXiv:2408.05292 [astro-ph.HE].
[4] P. Abreu et al. (Pierre Auger), Astrophys. J. **935**, 170 (2022), arXiv:2206.13492 [astro-ph.HE].
[5] T. Fujii, PoS **ICRC2023**, 031 (2024), arXiv:2401.08952 [astro-ph.HE].
[6] A. Aab et al. (Pierre Auger), Phys. Rev. D **102**, 062005 (2020), arXiv:2008.06486 [astro-ph.HE].
[7] A. Aab et al. (Pierre Auger), Phys. Rev. Lett. **125**, 121106 (2020), arXiv:2008.06488 [astro-ph.HE].
[8] S. Razzaque, APS Physics **13**, 145 (2020).
[9] F. Scherb, M.I.T. Nuclear Science Technical Report **71** (1959).
[10] G. W. Clark, J. Earl, W. L. Kraushaar, J. Linsley, B. B. Rossi, F. Scherb, and D. W. Scott, Phys. Rev. **122**, 637 (1961).
[11] M. Ave, J. A. Hinton, R. A. Vazquez, A. A. Watson, and E. Zas, Phys. Rev. Lett. **85**, 2244 (2000), arXiv:astro-ph/0007386.
[12] A. Aab et al. (Pierre Auger), JINST **15** (10), P10021, arXiv:2007.09035 [astro-ph.IM].
[13] M. Ave, R. A. Vazquez, and E. Zas, Astropart. Phys. **14**, 91 (2000), arXiv:astro-ph/0011490.
[14] A. Aab et al. (Pierre Auger), JCAP **08**, 019 (2014), arXiv:1407.3214 [astro-ph.HE].
[15] J. Hersil, I. Escobar, D. Scott, G. Clark, and S. Olbert, Phys. Rev. Lett. **6**, 22 (1961).
[16] A. Aab et al. (Pierre Auger), Phys. Rev. D **100**, 082003 (2019), arXiv:1901.08040 [astro-ph.IM].
[17] A. Aab et al. (Pierre Auger), JCAP **08**, 049 (2015), arXiv:1503.07786 [astro-ph.HE].
[18] H. P. Dembinski, P. Billoir, O. Deligny, and T. Hebbeker, Astropart. Phys. **34**, 128 (2010), arXiv:0904.2372 [astro-ph.IM].
[19] P. Abreu et al. (Pierre Auger), Eur. Phys. J. C **81**, 966 (2021), arXiv:2109.13400 [astro-ph.HE].
[20] V. Verzi et al. (Pierre Auger), in Proceedings of 33rd ICRC (2013) p. 0928.
[21] J. Abraham et al. (Pierre Auger), Nucl. Instrum. Meth. A **613**, 29 (2010), arXiv:1111.6764 [astro-ph.IM].
[22] C. K. Guerard et al. (Pierre Auger), in Proceedings of 27th ICRC (2002).

[23] P. Abreu et al. (Pierre Auger), Astropart. Phys. **34**, 368 (2011), arXiv:1010.6162 [astro-ph.HE].
[24] A. Abdul Halim et al. (Pierre Auger), Phys. Rev. Lett. **134**, 021001 (2025), arXiv:2406.06315 [astro-ph.HE].
[25] A. Abdul Halim et al. (Pierre Auger), Phys. Rev. D **111**, 022003 (2025), arXiv:2406.06319 [astro-ph.HE].
[26] M. Bonamente, J. Appl. Stat. **47**, 2044 (2020), arXiv:1912.05444 [astro-ph.HE].
[27] P. Abreu et al. (Pierre Auger), Astrophys. J. Suppl. **203**, 34 (2012), arXiv:1210.3736 [astro-ph.HE].
[28] P. L. Biermann and V. de Souza, Astrophys. J. **746**, 72 (2012), arXiv:1106.0625 [astro-ph.HE].
[29] A. Keivani, G. R. Farrar, and M. Sutherland, Astropart. Phys. **61**, 47 (2014), arXiv:1406.5249 [astro-ph.HE].
[30] A. R. Bell and J. H. Matthews, Mon. Not. Roy. Astron. Soc. **511**, 448 (2022), arXiv:2108.08879 [astro-ph.HE].
[31] S. Mollerach and E. Roulet, Phys. Rev. D **110**, 063030 (2024), arXiv:2406.19199 [astro-ph.HE].
[32] S. Marafico, J. Biteau, A. Condorelli, O. Deligny, and J. Bregeon, Astrophys. J. **972**, 4 (2024), arXiv:2405.17179 [astro-ph.HE].
[33] R. Mbarek, D. Caprioli, and K. Murase, Phys. Rev. D **111**, 023024 (2025), arXiv:2410.05696 [astro-ph.HE].
[34] G. E. Romero, A. L. Müller, and M. Roth, Astron. Astrophys. **616**, A57 (2018), arXiv:1801.06483 [astro-ph.HE].
[35] L. A. Anchordoqui and J. F. Soriano, PoS **ICRC2019**, 255 (2021), arXiv:1905.13243 [astro-ph.HE].
[36] R. U. Abbasi et al. (Telescope Array), (2024), arXiv:2406.08612 [astro-ph.HE].
[37] A. A. Halim et al. (Pierre Auger), JCAP **05**, 024, arXiv:2211.02857 [astro-ph.HE].
[38] D. Ehlert, F. Oikonomou, and M. Unger, Phys. Rev. D **107**, 103045 (2023), arXiv:2207.10691 [astro-ph.HE].
[39] G. R. Farrar, Phys. Rev. Lett. **134**, 081003 (2025), arXiv:2405.12004 [astro-ph.HE].
[40] B. T. Zhang, K. Murase, N. Ekanger, M. Bhattacharya, and S. Horiuchi, (2024), arXiv:2405.17409 [astro-ph.HE].
[41] A. Aab et al. (Pierre Auger), (2016), arXiv:1604.03637 [astro-ph.IM].
[42] B. R. Dawson et al. (Pierre Auger), EPJ Web Conf. **197**, 01004 (2019).
[43] V. M. Harvey et al. (Pierre Auger), PoS **ICRC2023**, 300 (2023).
[44] J. Bellido et al. (Pierre Auger), PoS **ICRC2023**, 211 (2023).
[45] A. Aab et al. (Pierre Auger), Phys. Rev. D **90**, 122005 (2014), arXiv:1409.4809 [astro-ph.HE].
[46] J. Matthews, Astropart. Phys. **22**, 387 (2005).
[47] T. Pierog, I. Karpenko, J. M. Katzy, E. Yatsenko, and K. Werner, Phys. Rev. C **92**, 034906 (2015), arXiv:1306.0121 [hep-ph].
[48] L. Cazon, R. Conceição, and F. Riehn, Phys. Lett. B **784**, 68 (2018), arXiv:1803.05699 [hep-ph].
[49] C. Bérat, C. Bleve, O. Deligny, F. Montanet, P. Savina, and Z. Torrès, Astrophys. J. **929**, 55 (2022), arXiv:2203.08751 [astro-ph.HE].
[50] C. Berat, A. Condorelli, O. Deligny, F. Montanet, and Z. Torres, Astrophys. J. **966**, 186 (2024), arXiv:2402.04759 [astro-ph.HE].

END MATTER

In this appendix, we first provide details of the energy-calibration of S_{38} and of N_{68}, and then explain the sources of energy-dependent systematic uncertainties in N_{68} that enter into the budget σ_C and justify the use of a non-zero δC above 10 EeV.

Table II. Coefficients of the second-degree polynomial in terms of $y_S = \log_{10}(S_{38}/(40\ \mathrm{VEM}))$ for the parameters a_S, b_S and c_S.

	y_S^0	y_S^1	y_S^2
a_S	0.936	0.005	−0.400
b_S	−1.62	−0.51	−0.13
c_S	−0.92	0.54	1.75

The energy calibration of $S(1000)$ is derived from a two-step process [6]. Firstly, $S(1000)$ is corrected for attenuation effects with zenith angle θ by using the Constant Intensity Cut method [15]. For a given intensity threshold, the attenuation curve is fitted with a third-degree polynomial, $S(1000) = S_{38}(1 + a_S x_S + b_S x_S^2 + c_S x_S^3)$, where $x_S = \cos^2\theta - \cos^2 38°$ and S_{38} is a zenith-independent shower-size estimator. The intensity-threshold dependence in the curves is accounted for by introducing an empirical dependence in terms of $y_S = \log_{10}(S_{38}/40\ \mathrm{VEM})$ in the coefficients a_S, b_S and c_S through a second-order polynomial in y. A VEM corresponds to the energy deposit of one vertical equivalent muon. The polynomial coefficients, updated with respect to those in [6], are given in Table II. They relate to S_{38} values ranging from 15 VEM to 120 VEM. Outside these bounds, the coefficients are set to their values at 15 and 120 VEM. Secondly, the corrected shower-size estimator, S_{38}, is converted into energy E using a power-law calibration relationship, $E = A_S(S_{38})^{B_S}$, determined with high-quality events detected simultaneously with the fluorescence detector. The energy scale is based on [42], with recent improvements concerning aerosol attenuation [43] and longitudinal-profile reconstruction [44]. In this study, $A_S = (1.86 \pm 0.03) \times 10^{-1}$ EeV and $B_S = 1.021 \pm 0.004$.

Table III. Coefficients of the first-degree polynomial in terms of $y_N = \log_{10} N_{19}$) for the parameters a_N and b_N.

	y_N^0	y_N^1
a_N	−0.292	0.468
b_N	−4.96	0.79

The energy calibration of N_{19} is carried out in the same manner. A constant-intensity-cut correction is applied to the (relative) muon-number estimator N_{19} using a second-degree polynomial, $N_{19} = N_{68}(1 + a_N x_N + b_N x_N^2)$, which is enough to guarantee the same intensity in bins of $\cos^2\theta$ between 60° and 80° (with $x_N = \cos^2\theta - \cos^2 68°$). The intensity-threshold dependence is accounted for by introducing an empirical dependence in terms of $y_N = \log_{10}(N_{19})$ in the coefficients a_N and b_N. The polynomial coefficients are given in Table III. They relate to N_{68} values ranging from 0.9 to 4.5. Outside these bounds, the coefficients are set to their values at 0.9 and 4.5. The energy-calibration relationship is $E = A_N(N_{68})^{B_N}$, with $A_N = (5.29 \pm 0.06)$ EeV and $B_N = 1.046 \pm 0.014$. Note that these values are refereed to as $A \pm \sigma_A$ and $B \pm \sigma_B$ in the main text.

Since N_{68} depends on the mass composition of the primary

particles, its calibration relationship to the energy measured with the fluorescence technique accounts for the trend of the composition change with energy inherently as the underlying mass distribution is directly sampled by the fluorescence detectors. The use of a single power law for the relationship between N_{68} and E is then justified only for a single logarithmic evolution of the composition as a function of energy. This turns out to be the case, within the statistical uncertainties of the fluorescence dataset, above $\simeq 2$ EeV [45]. However, using deep-neural-network techniques applied to the surface-detector dataset, sharp changes of the elongation rate, too small to show up within the statistics available with the fluorescence technique, have recently been uncovered around $\simeq 6$ EeV, $\simeq 10$ EeV and $\simeq 30$ EeV [24, 25]. The impact of these elongation rate changes on the energy calibration of N_{68} can be estimated as follows. Within the Heitler-Matthews superposition model of air shower [46], the number of muons N_μ increases with the cosmic-ray mass number A as $N_\mu \propto A^{1-\beta}$. Assuming that the slope of N_{68} with A follows that of N_μ, the change of slope of N_{68}, $\Delta m_{N_{68}}$, can be related to that of the shower maximum slant depth, $\Delta m_{X_{\rm max}}$ through

$$\Delta m_{N_{68}} = -\frac{1-\beta}{D_0}\Delta m_{X_{\rm max}}, \tag{7}$$

with $D_0 \simeq 56.1$ g cm^{-2} the elongate rate of protons expected from EPOS-LHC [47]. Using $\beta \simeq 0.927$ as a benchmark [48], and considering to first order a single change of elongation rate around 10 EeV to describe the observed series of kinks from below 6 EeV to above 30 EeV, we get an amplitude for the expected non-linearity of N_{68} of $\simeq 2.5\%$ per decade. We note that we neglect here the correlated non-linearity effects in the energy calibration of S_{38} as they are smaller.

Another source of logarithmic non-linearities between N_{68} and E stems from the use of the constant-intensity-cut correction to make uniform the distribution of events in terms of $\sin^2\theta$. The correction is necessary to compensate for imperfections of the N_{19} energy estimator, which accounts for muon contributions to the signals and requires model-dependent corrections for electromagnetic ones, not negligible between $\theta = 60°$ and $\theta \simeq 70°$. However, smaller, yet genuine, deviations of the $\sin^2\theta$ distribution from uniformity, Δ, are expected in presence of dipolar anisotropies. They can be estimated as [27]

$$\Delta = \frac{N_{\rm dip}}{N_{\rm iso}} d_z \sin\lambda \cos\theta, \tag{8}$$

with $N_{\rm iso}$ ($N_{\rm dip}$) the expected number of events in the covered region of the sky for an isotropic (a dipolar) angular distribution. While Δ is well within 1% for $\theta \leq 60°$ for the dipole components d_z of interest (measured with large uncertainties, though), it increases up to, on average, $\simeq 3\%$ for $\theta \geq 60°$. We estimated that the uniformity of the $\sin^2\theta$ distribution forced by the constant intensity correction for $N_{68} < 4.5$ ($E \simeq 20$ EeV) can then lead to energy distortions of $\simeq 1.5\%$ between 4 and $\simeq 20$ EeV, while higher energies would not be impacted as the energy dependence of the polynomial coefficients relating N_{19} to N_{68} is frozen. This effectively acts as a source of non-linearity that occurs around $\simeq 20$ EeV.

Overall, we add in quadrature both sources of non-linearities and end up with $\sigma_C = 3\times10^{-2}$, and choose, as a first-order approximation, the transition energy at 10 EeV. We have checked that the best-fit value for δC is mildly impacted when increasing σ_C to 5×10^{-2} or increasing the transition energy.

SUPPLEMENTAL MATERIAL

We provide in this supplemental material a few summary plots and data related to the analysis presented in the article.

The response function for events between 0 and 60° is described in detail in our previous paper [6]. We have applied the same data-driven techniques to determine that for events between 60° and 80°. The resolution function is parameterized as a Gaussian function with σ_N parameter evolving with energy as

$$\frac{\sigma_N(E)}{E} = 0.046 + \frac{0.34}{\sqrt{E}}, \tag{9}$$

with E in EeV. No significant bias is found in the sub-threshold energy bins of interest, down to 2.5 EeV. The efficiency is described as (still with E in EeV)

$$\epsilon(E) = 0.5\left(1 + {\rm erf}\left(\frac{\log_{10}E}{0.34}\right)\right). \tag{10}$$

In Fig. 4, we present an alternative version of the bottom panel of Fig. 2. Here, the energy-spectra residuals in the five declination bands are zoomed within ±25% while no artificial shifts are applied for visualization purpose; some data points at high energies therefore lie outside the windows. The reference

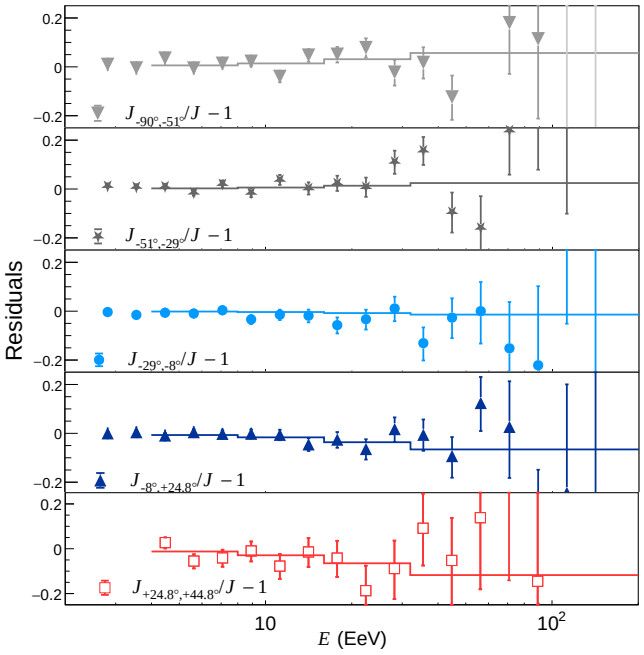


Figure 4. Energy-spectra residuals zoomed within ±25% in the five declination bands.

Table IV. Correlation matrix relative to $\mathbf{\Sigma}_{\rm ref}$ expressed in a basis $(J_0, \gamma_1, E_{12}, \gamma_2, E_{23}, \gamma_3, E_{34}, \gamma_4)$.

1.000	−0.535	+0.613	−0.396	−0.162	+0.218	−0.182	−0.317
	1.000	−0.782	+0.494	+0.343	+0.111	+0.561	+0.512
		1.000	−0.872	−0.609	−0.186	−0.329	−0.303
			1.000	+0.827	+0.313	+0.104	+0.052
				1.000	+0.594	+0.007	−0.052
					1.000	+0.133	−0.186
						1.000	+0.431
							1.000

lines are the best-fit function for the spectrum combined over $[-84.8°, +24.8°]$ accounting for dipole anisotropies.

The correlation matrix relative to the covariance matrices used to search for differences in the spectral features is given in Table IV. It provides, together with the corresponding uncertainties in the parameters listed in Table I, the coefficients needed to get $\mathbf{\Sigma}_{\rm ref}$ as well as $\mathbf{\Sigma}_{\Delta\delta}$.

The combined spectrum data points with their statistical and systematic uncertainties are collected in Table V together with the observed and corrected number of events, while the correlation matrix of the spectrum data points that accounts for systematic uncertainties is given in Table VI. The strong bin-to-bin correlations observed stem from systematic uncertainties dominated by those in the energy scale: for a single power-law spectrum in $E^{-\gamma}$, a $\Delta E/E$ change in energy scale translates indeed as a change $\Delta J(E)/J(E) = (\gamma - 1)\Delta E/E$. The correlation matrix together with the uncertainties collected in Table V allow for a direct model/data comparison through a generalized χ^2 that accounts for all sources of uncertainties. It can also be used to propagate uncertainties in any quantity derived from the cosmic-ray spectrum, such as cosmogenic gamma-ray [49] or neutrino fluxes [50].

Finally, the spectra obtained in each declination band are collected in Tables VII-to-XI.

Table V. Combined spectrum data.

$\log_{10}(E/\mathrm{EeV})$	$J(E) \pm \sigma_{\mathrm{stat}}(E) \pm \sigma_{\mathrm{syst}}(E)$ (EeV^{-1} km^{-2} sr^{-1} yr^{-1})	n	n_{corr}
0.45	$\left(1.8614\ ^{+0.0065\ +0.7}_{-0.0065\ -0.6}\right)\times10^{0}$	107232	98178.2
0.55	$\left(8.808\ ^{+0.040\ +3.2}_{-0.040\ -2.5}\right)\times10^{-1}$	61873	58483.8
0.65	$\left(4.183\ ^{+0.022\ +1.4}_{-0.022\ -1.1}\right)\times10^{-1}$	48929	45207.8
0.75	$\left(2.107\ ^{+0.014\ +0.6}_{-0.014\ -0.4}\right)\times10^{-1}$	30525	28678.2
0.85	$\left(1.186\ ^{+0.009\ +0.3}_{-0.009\ -0.3}\right)\times10^{-1}$	20984	20314.9
0.95	$\left(6.590\ ^{+0.059\ +1.5}_{-0.059\ -1.4}\right)\times10^{-2}$	14590	14213.9
1.05	$\left(3.668\ ^{+0.039\ +0.9}_{-0.039\ -0.8}\right)\times10^{-2}$	10159	9957.9
1.15	$\left(2.001\ ^{+0.024\ +0.5}_{-0.026\ -0.6}\right)\times10^{-2}$	6984	6858.1
1.25	$\left(9.982\ ^{+0.152\ +3.0}_{-0.165\ -2.8}\right)\times10^{-3}$	4396	4296.4
1.35	$\left(5.027\ ^{+0.097\ +1.5}_{-0.101\ -1.3}\right)\times10^{-3}$	2775	2724.0
1.45	$\left(2.600\ ^{+0.062\ +0.7}_{-0.067\ -0.7}\right)\times10^{-3}$	1800	1773.7
1.55	$\left(1.294\ ^{+0.039\ +0.4}_{-0.043\ -0.3}\right)\times10^{-3}$	1124	1112.3
1.65	$\left(5.88\ ^{+0.23\ +2.7}_{-0.26\ -2.4}\right)\times10^{-4}$	634	635.3
1.75	$\left(2.27\ ^{+0.13\ +1.2}_{-0.14\ -1.1}\right)\times10^{-4}$	318	309.3
1.85	$\left(6.98\ ^{+0.67\ +5.3}_{-0.69\ -3.4}\right)\times10^{-5}$	126	119.5
1.95	$\left(1.89\ ^{+0.29\ +1.9}_{-0.32\ -0.6}\right)\times10^{-5}$	43	40.8
2.05	$\left(5.3\ ^{+1.4\ +6.0}_{-1.6\ -2.8}\right)\times10^{-6}$	15	14.2
2.15	$\left(2.5\ ^{+0.7\ +0.1}_{-1.1\ -1.9}\right)\times10^{-6}$	9	8.5
2.25	$< 5.4\times10^{-7}$	0	0
2.35	$< 4.3\times10^{-7}$	0	0

Table VI. Correlation matrix of the spectrum accounting for systematic uncertainties.

i \ j	0.45	0.55	0.65	0.75	0.85	0.95	1.05	1.15	1.25	1.35	1.45	1.55	1.65	1.75	1.85	1.95	2.05	2.15
0.45	1	0.984	0.983	0.980	0.985	0.991	0.986	0.976	0.971	0.970	0.980	0.987	0.990	0.983	0.974	0.946	0.957	0.788
0.55		1	0.999	0.999	0.993	0.993	0.986	0.977	0.978	0.977	0.981	0.986	0.990	0.997	0.994	0.973	0.963	0.848
0.65			1	0.999	0.994	0.993	0.984	0.975	0.977	0.975	0.983	0.987	0.991	0.997	0.994	0.972	0.962	0.853
0.75				1	0.993	0.991	0.982	0.970	0.971	0.970	0.978	0.987	0.989	0.997	0.994	0.974	0.960	0.851
0.85					1	0.997	0.986	0.977	0.967	0.965	0.986	0.996	0.997	0.992	0.982	0.949	0.955	0.859
0.95						1	0.992	0.985	0.977	0.974	0.986	0.994	0.994	0.990	0.981	0.953	0.951	0.842
1.05							1	0.994	0.991	0.989	0.980	0.985	0.982	0.976	0.971	0.945	0.949	0.805
1.15								1	0.993	0.992	0.981	0.973	0.974	0.964	0.958	0.924	0.941	0.813
1.25									1	0.998	0.976	0.964	0.963	0.964	0.965	0.943	0.937	0.803
1.35										1	0.973	0.961	0.963	0.962	0.962	0.942	0.943	0.787
1.45											1	0.986	0.984	0.974	0.963	0.922	0.941	0.850
1.55												1	0.993	0.983	0.974	0.937	0.944	0.842
1.65													1	0.989	0.978	0.946	0.962	0.832
1.75														1	0.994	0.974	0.959	0.852
1.85															1	0.981	0.949	0.849
1.95																1	0.923	0.785
2.05																	1	0.756
2.15																		1

Table VII. Spectrum data over the declination band $[-90°, -51°]$.

$\log_{10}(E/\mathrm{EeV})$	$J(E) \pm \sigma_{\mathrm{stat}}(E)$ (EeV^{-1} km^{-2} sr^{-1} yr^{-1})	n	n_{corr}
0.45	$\left(1.875\ ^{+0.013}_{-0.013}\right) \times 10^{0}$	24889	22728.5
0.55	$\left(8.797\ ^{+0.082}_{-0.081}\right) \times 10^{-1}$	14198	13424.9
0.65	$\left(4.294\ ^{+0.041}_{-0.045}\right) \times 10^{-1}$	11557	10693.2
0.75	$\left(2.114\ ^{+0.026}_{-0.028}\right) \times 10^{-1}$	7045	6628.6
0.85	$\left(1.194\ ^{+0.017}_{-0.019}\right) \times 10^{-1}$	4873	4714.3
0.95	$\left(6.793\ ^{+0.116}_{-0.126}\right) \times 10^{-2}$	3470	3375.1
1.05	$\left(3.549\ ^{+0.075}_{-0.082}\right) \times 10^{-2}$	2278	2220.4
1.15	$\left(2.104\ ^{+0.052}_{-0.057}\right) \times 10^{-2}$	1685	1657.4
1.25	$\left(1.057\ ^{+0.032}_{-0.035}\right) \times 10^{-2}$	1057	1048.1
1.35	$\left(5.49\ ^{+0.21}_{-0.22}\right) \times 10^{-3}$	699	684.7
1.45	$\left(2.48\ ^{+0.13}_{-0.14}\right) \times 10^{-3}$	397	389.4
1.55	$\left(1.30\ ^{+0.08}_{-0.09}\right) \times 10^{-3}$	263	258.0
1.65	$\left(5.54\ ^{+0.49}_{-0.52}\right) \times 10^{-4}$	141	137.9
1.75	$\left(2.78\ ^{+0.30}_{-0.31}\right) \times 10^{-4}$	85	86.8
1.85	$\left(7.7\ ^{+1.4}_{-1.6}\right) \times 10^{-5}$	31	30.3
1.95	$\left(2.1\ ^{+0.7}_{-0.7}\right) \times 10^{-5}$	12	10.4
2.05	$\left(1.4\ ^{+1.8}_{-1.2}\right) \times 10^{-6}$	1	0.9
2.15	$\left(1.1\ ^{+1.4}_{-0.9}\right) \times 10^{-6}$	1	0.9
2.25	$< 2.0 \times 10^{-6}$	0	0
2.35	$< 1.6 \times 10^{-6}$	0	0

Table VIII. Spectrum data over the declination band $[-51°, -29°]$.

$\log_{10}(E/\mathrm{EeV})$	$J(E) \pm \sigma_{\mathrm{stat}}(E)$ (EeV^{-1} km^{-2} sr^{-1} yr^{-1})	n	n_{corr}
0.45	$\left(1.881\ ^{+0.012}_{-0.012}\right) \times 10^{0}$	29491	27226.2
0.55	$\left(8.921\ ^{+0.076}_{-0.076}\right) \times 10^{-1}$	17193	16258.8
0.65	$\left(4.192\ ^{+0.039}_{-0.043}\right) \times 10^{-1}$	12052	11194.9
0.75	$\left(2.095\ ^{+0.025}_{-0.027}\right) \times 10^{-1}$	7509	7044.0
0.85	$\left(1.202\ ^{+0.017}_{-0.019}\right) \times 10^{-1}$	5247	5088.8
0.95	$\left(6.544\ ^{+0.110}_{-0.119}\right) \times 10^{-2}$	3565	3487.2
1.05	$\left(3.836\ ^{+0.075}_{-0.082}\right) \times 10^{-2}$	2616	2573.7
1.15	$\left(2.015\ ^{+0.048}_{-0.052}\right) \times 10^{-2}$	1743	1702.3
1.25	$\left(1.030\ ^{+0.031}_{-0.033}\right) \times 10^{-2}$	1118	1095.3
1.35	$\left(5.13\ ^{+0.20}_{-0.21}\right) \times 10^{-3}$	697	686.8
1.45	$\left(2.82\ ^{+0.13}_{-0.14}\right) \times 10^{-3}$	479	474.8
1.55	$\left(1.48\ ^{+0.08}_{-0.09}\right) \times 10^{-3}$	313	314.9
1.65	$\left(5.72\ ^{+0.46}_{-0.48}\right) \times 10^{-4}$	157	152.9
1.75	$\left(1.84\ ^{+0.24}_{-0.24}\right) \times 10^{-4}$	65	62.0
1.85	$\left(8.1\ ^{+1.4}_{-1.5}\right) \times 10^{-5}$	35	34.2
1.95	$\left(2.7\ ^{+0.8}_{-0.7}\right) \times 10^{-5}$	15	14.7
2.05	$\left(7.3\ ^{+3.2}_{-2.8}\right) \times 10^{-6}$	5	4.9
2.15	$\left(5.8\ ^{+2.5}_{-2.3}\right) \times 10^{-6}$	5	4.9
2.25	$< 2.1 \times 10^{-6}$	0	0
2.35	$< 1.7 \times 10^{-6}$	0	0

Table IX. Spectrum data over the declination band $[-29°, -8°]$.

$\log_{10}(E/\mathrm{EeV})$	$J(E) \pm \sigma_{\mathrm{stat}}(E)$ (EeV^{-1} km^{-2} sr^{-1} yr^{-1})	n	n_{corr}
0.45	$\left(1.850\,^{+0.012}_{-0.012}\right)\times10^{-0}$	28269	25961.0
0.55	$\left(8.703\,^{+0.076}_{-0.076}\right)\times10^{-1}$	16303	15376.7
0.65	$\left(4.119\,^{+0.039}_{-0.043}\right)\times10^{-1}$	11529	10677.9
0.75	$\left(2.105\,^{+0.025}_{-0.027}\right)\times10^{-1}$	7258	6870.6
0.85	$\left(1.182\,^{+0.017}_{-0.018}\right)\times10^{-1}$	5003	4854.1
0.95	$\left(6.420\,^{+0.111}_{-0.119}\right)\times10^{-2}$	3408	3319.7
1.05	$\left(3.642\,^{+0.075}_{-0.080}\right)\times10^{-2}$	2420	2371.2
1.15	$\left(1.972\,^{+0.049}_{-0.054}\right)\times10^{-2}$	1646	1615.9
1.25	$\left(9.482\,^{+0.296}_{-0.323}\right)\times10^{-3}$	1001	978.3
1.35	$\left(4.92\,^{+0.19}_{-0.21}\right)\times10^{-3}$	651	639.1
1.45	$\left(2.56\,^{+0.13}_{-0.14}\right)\times10^{-3}$	425	419.0
1.55	$\left(1.11\,^{+0.07}_{-0.08}\right)\times10^{-3}$	232	229.3
1.65	$\left(6.15\,^{+0.49}_{-0.52}\right)\times10^{-4}$	159	159.4
1.75	$\left(2.19\,^{+0.26}_{-0.29}\right)\times10^{-4}$	73	71.5
1.85	$\left(5.5\,^{+1.0}_{-1.1}\right)\times10^{-5}$	24	22.7
1.95	$\left(1.5\,^{+0.5}_{-0.5}\right)\times10^{-5}$	8	7.5
2.05	$\left(8.7\,^{+3.6}_{-4.1}\right)\times10^{-6}$	6	5.7
2.15	$\left(1.2\,^{+1.3}_{-1.0}\right)\times10^{-6}$	1	0.9
2.25	$< 2.2\times10^{-6}$	0	0
2.35	$< 1.7\times10^{-6}$	0	0

Table X. Spectrum data over the declination band $[-8°, +24.8°]$.

$\log_{10}(E/\mathrm{EeV})$	$J(E) \pm \sigma_{\mathrm{stat}}(E)$ (EeV^{-1} km^{-2} sr^{-1} yr^{-1})	n	n_{corr}
0.45	$\left(1.857\ ^{+0.013}_{-0.013}\right) \times 10^{0}$	24477	22123.1
0.55	$\left(8.880\ ^{+0.083}_{-0.083}\right) \times 10^{-1}$	14109	13320.9
0.65	$\left(4.109\ ^{+0.039}_{-0.043}\right) \times 10^{-1}$	11712	10776.8
0.75	$\left(2.136\ ^{+0.025}_{-0.028}\right) \times 10^{-1}$	7523	7055.6
0.85	$\left(1.175\ ^{+0.017}_{-0.018}\right) \times 10^{-1}$	5048	4885.2
0.95	$\left(6.632\ ^{+0.111}_{-0.122}\right) \times 10^{-2}$	3560	3471.6
1.05	$\left(3.673\ ^{+0.074}_{-0.080}\right) \times 10^{-2}$	2464	2420.3
1.15	$\left(1.918\ ^{+0.048}_{-0.053}\right) \times 10^{-2}$	1634	1591.4
1.25	$\left(9.796\ ^{+0.305}_{-0.327}\right) \times 10^{-3}$	1049	1023.0
1.35	$\left(4.76\ ^{+0.19}_{-0.21}\right) \times 10^{-3}$	638	625.9
1.45	$\left(2.57\ ^{+0.12}_{-0.14}\right) \times 10^{-3}$	433	426.6
1.55	$\left(1.27\ ^{+0.07}_{-0.08}\right) \times 10^{-3}$	269	265.4
1.65	$\left(5.72\ ^{+0.45}_{-0.51}\right) \times 10^{-4}$	150	150.2
1.75	$\left(2.46\ ^{+0.26}_{-0.28}\right) \times 10^{-4}$	82	81.4
1.85	$\left(6.7\ ^{+1.3}_{-1.4}\right) \times 10^{-5}$	30	27.8
1.95	$\left(1.0\ ^{+0.5}_{-0.5}\right) \times 10^{-5}$	6	5.5
2.05	$\left(4.2\ ^{+1.9}_{-2.7}\right) \times 10^{-6}$	3	2.8
2.15	$\left(2.2\ ^{+1.4}_{-2.1}\right) \times 10^{-6}$	2	1.8
2.25	$< 2.0 \times 10^{-6}$	0	0
2.35	$< 1.6 \times 10^{-6}$	0	0

Table XI. Spectrum data over the declination band $[+24.8°, +44.8°]$.

$\log_{10}(E/\mathrm{EeV})$	$J(E) \pm \sigma_{\mathrm{stat}}(E)$ (EeV^{-1} km^{-2} sr^{-1} yr^{-1})	n	n_{corr}
0.65	$\left(4.259\ ^{+0.100}_{-0.109}\right)\times10^{-1}$	2037	1793.8
0.75	$\left(2.008\ ^{+0.061}_{-0.066}\right)\times10^{-1}$	1172	1064.9
0.85	$\left(1.13\ ^{+0.04}_{-0.04}\right)\times10^{-1}$	793	753.6
0.95	$\left(6.58\ ^{+0.28}_{-0.31}\right)\times10^{-2}$	574	552.7
1.05	$\left(3.41\ ^{+0.18}_{-0.19}\right)\times10^{-2}$	371	360.6
1.15	$\left(1.98\ ^{+0.13}_{-0.13}\right)\times10^{-2}$	270	263.7
1.25	$\left(9.63\ ^{+0.74}_{-0.81}\right)\times10^{-3}$	167	161.6
1.35	$\left(4.13\ ^{+0.46}_{-0.49}\right)\times10^{-3}$	90	87.3
1.45	$\left(2.31\ ^{+0.29}_{-0.31}\right)\times10^{-3}$	63	61.4
1.55	$\left(1.4\ ^{+0.2}_{-0.2}\right)\times10^{-3}$	48	46.8
1.65	$\left(6.0\ ^{+1.1}_{-1.2}\right)\times10^{-4}$	26	25.2
1.75	$\left(2.5\ ^{+0.75}_{-0.8}\right)\times10^{-4}$	13	13.2
1.85	$\left(9.1\ ^{+4.3}_{-4.6}\right)\times10^{-5}$	6	6.1
1.95	$\left(1.6\ ^{+0.8}_{-1.4}\right)\times10^{-5}$	2	1.3
2.05	$< 1.2\times10^{-5}$	0	0
2.15	$< 9.8\times10^{-6}$	0	0
2.25	$< 8.0\times10^{-6}$	0	0
2.35	$< 6.5\times10^{-6}$	0	0